Digital Object Identifier 10.1109/TPEL.2024.3354409

IEEE Transactions on Power Electronics

Sub-synchronous Damping by Battery Storage System in Grid-Forming Control

Ziqi Zhou
Sante Pugliese
Marius Langwasser
Marco Liserre

Suggested Citation

Z. Zhou, S. Pugliese, M. Langwasser and M. Liserre, "Subsynchronous Damping by Battery Storage System in Grid-Forming Control," in IEEE Transactions on Power Electronics, vol. 39, no. 4, pp. 4173-4186, April 2024.

Sub-Synchronous Damping by Battery Storage System in Grid Forming Control

Ziqi Zhou, *Graduate Student Member, IEEE*, Sante Pugliese, *Member, IEEE*, Marius Langwasser, *Member, IEEE*, and Marco Liserre, *Fellow, IEEE*

***Abstract*—Wind farms are susceptible to sub-synchronous oscillation (SSO) issues due to the interaction between the grid-side converter (GSC) and the weak-grid impedance. Integration of battery energy storage system (BESS) to damp SSO became popular due to its ability to also provide various grid services. Generally, BESS can be externally integrated at the PCC or internally integrated at the dc-link of the wind turbine (WT). In case of external BESS integration, grid-forming (GFM) control is usually applied to the BESS GSC. Proper increase of the GFM damping coefficient contributes to a better SSO damping, at the cost of a higher BESS power rating due to its droop meaning. Reconfiguring power loop of GFM to decouple the damping and the droop coefficient enables GSC to realize similar SSO damping performance while reducing the BESS power rating. In case of internal BESS integration, a virtual grid-forming control is proposed as an ancillary control of the WT GSC. This enables GSC to emulate the output behavior of two parallel converters, operated in grid-following and GFM mode respectively. Consequently, similar SSO damping performance can be realized without an external GFM converter. Simulation and experimental results are provided to verify the effectiveness of the proposed method.**

***Index Terms*—BESS, grid-forming control, sub-synchronous oscillation damping, wind power.**

I. Introduction

With the increasing penetration of power electronics based renewable energy sources (e.g. PV and wind farms), the power system is more susceptible to sub-synchronous oscillations (SSO) issues. In a wind farm, sub-synchronous oscillations can be classified into three types based on their generation and interaction mechanism: DFIG-series capacitor interaction (DFIG-SSR), Converter-grid interaction (CGI), and Converter-converter interaction (CCI) [1]. The CGI usually occurs when renewable energy sources are connected to a weak-grid [2]. In this scenario, the grid-side converter (GSC) of wind turbine generator behaves as a capacitive impedance with negative damping in the low frequency region. Therefore, when the GSC is connected to a weak-grid (i.e. grid with high equivalent line impedance), low frequency resonances might be generated [3]. Many approaches have been already investigated in literature to damp the SSO caused by CGI and they can be roughly categorized into two types.

The first type is to redesign the control parameters or the structure of the wind turbine (WT) control system considering the SSO phenomena. To this extent, research results in [4] studied the effect of dc-link voltage control bandwidth on the sub-synchronous interaction (SSI) mode. By properly designing the parameters of the dc-link voltage controller, the SSI damping can be improved. [5] showed that the eigenvalues related to the SSO are sensitive to the proportional gain of the PLL in the GSC, and decreasing it can improve the stability margin. However, the PLL parameters are generally designed to meet grid codes such as fault ride-through (FRT) ability and dynamic requirements. Therefore, it is not practical to change the PLL control parameters. Meanwhile, the development of grid-forming (GFM) control structure in the GSC of D-PMSG wind turbines [6], [7] provided additional possibilities for SSO damping. Unlike conventional grid-following (GFL) controlled converters [8], GFM converters do not require a synchronization unit, such as PLL, to estimate the amplitude and the angle of the grid voltage and they can realize self-synchronization instead. With the GFM control, the SSO mode generated by the PLL can be avoided. Although GFM control shows better stability performance than GFL control against such kind of SSO, issues like current limiting under grid fault conditions and synchronization stability remain a concern to be further investigated [9].

The second type consists in the installation of external flexible ac transmission systems (FACTS) into the wind farm. In [10], a STATCOM in reactive power control mode is recommended to damp the CGI. However, [11] reported a phenomenon of CCI based SSO caused by the integration of STATCOMs into power system. Besides, main drawbacks of commissioning FACTS for SSO damping are that it requires capital intensive investments [1]. Therefore, the combination of GFM control and BESS became popular recently not only for SSO damping purpose [12] but also for offering grid services such as frequency support and black-start service in off-shore wind farms [13]. A realistic example on how GFM based BESS contributes to a range grid services is reported in [14]. For SSO damping by means of external GFM based BESS, in [12], a GFM control structure called virtual synchronous generator (VSG) is applied. In [15], it is shown that VSG based BESS performs as a voltage source behind an inductive impedance. Therefore, when the BESS is integrated at the PCC point of the WT, the equivalent impedance obtained from paralleling the grid and the output BESS impedance is smaller than the standalone grid impedance. This reduces the equivalent grid impedance from the view of the WT. As a result, the SSO can be damped due to an improved grid stiffness. The relationship between SSO damping performance

Ziqi Zhou, Sante Pugliese, Marius Langwasser and Marco Liserre are with the Chair of Power Electronics, Kiel University, 24143 Kiel, Germany (e-mail: ziqi,sapu,mlan,ml@tf.uni-kiel.de).

Marco Liserre is also with the Fraunhofer Institute for Silicon Technology ISIT, Fraunhoferstr. 1, 25524 Itzehoe, Germany (e-mail: marco.liserre@isit.fraunhofer.de).

and damping coefficient of VSG is in further investigated in [16], indicating that the SSO can be better damped when the damping coefficient is properly increased. Since the damping coefficient generally represents also for the droop coefficient [17], under frequency deviation and especially under frequency drop conditions, a large power rated BESS is required with the drawback of increasing costs [17]. Therefore, a control technique to decouple the damping and droop coefficients in conventional VSG is proposed by the authors in [16]. Consequently, the damping coefficient can be designed with larger values to better damp SSO and the droop characteristic can be set smaller to reduce the battery power rating. The details on the SSO contribution from the decoupling control will be introduced in the later section.

Since the external GFM based BESS contributes to the SSO by changing the equivalent grid impedance seen by the WT at the PCC, the BESS should be installed as closer as possible to the WT if good SSO damping is expected. In this scenario, [18] discussed the potential to directly integrate the BESS inside the WT. The BESS shares the dc-link with the GSC of the WT, which generally operates in GFL mode. However, in [18], the BESS is only proposed as a solution to the intermittent nature of the wind power generation, while the SSO damping and grid services like frequency support are not discussed. Since in this condition, there is no additional GFM converter connected in parallel to the WT converter operated in GFL mode, SSO could arise if the WT is not properly controlled.

The main contributions of the paper are:

1. For the case of external GFM BESS integration, A coefficient decoupling control is proposed for the GFM control to reduce the battery power rating requirement while keeping similar SSO damping behavior ;
2. A generic parameters design method of the proposed decoupling control is provided;
3. For the case of internal BESS integration, A virtual grid-forming control (VGFMC) is proposed, which enables WT GSC to emulate the SSO damping behavior of the external GFM converter; VGFMC can be regarded as an ancillary control for the GFL control of the WT GSC, which does not change the control structure of the GFL control and can be flexibly switched.

The rest of the paper is organized as follow: in Section II, the grid-connected system of a wind farm is introduced, and the SSO issue caused by CGI is discussed. In Section III, the coefficient decoupling control is introduced for the conventional VSG to decouple the damping coefficient and the droop coefficient. In Section IV, the VGFMC is presented and compared with the conventional parallel GFL and GFM converters. In Section V, experimental results are provided to verify the effectiveness of the proposed method. Finally, Section VI concludes the paper.

II. Grid-Connected Wind Turbine Under Weak-Grid Conditions

Fig. 1 shows the structure of a grid-connected D-PMSG based WT which consists of a PMSG, a back-to-back converter, filter, transformers, transmission line and the grid. The

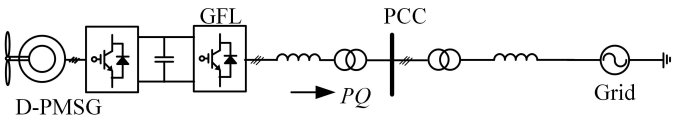

Fig. 1. Structure of a D-PMSG based single wind turbine grid-connected system.

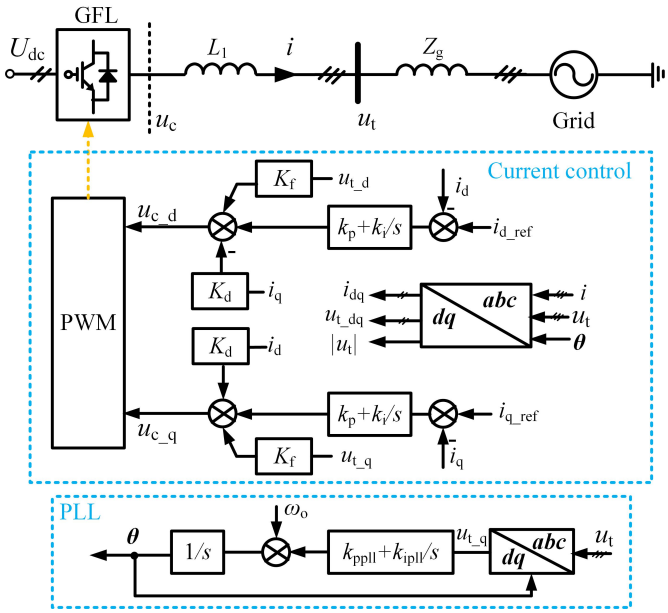

Fig. 2. Simplified control system of the WT grid-side converter.

WT regulates the output active power P and the reactive power Q injected into the grid through the GSC, which generally operates in GFL control mode, as shown in Fig. 2. Here, the WT generator-side dynamic is neglected and substituted with a constant dc-source to simplify the analysis. The basic principle of a GFL control is to regulate the converter output power by controlling the converter output currents, typically in a rotating dq-frame. The current control generally requires a synchronization unit, such as PLL, to synchronize itself with the PCC voltage for abc-dq transformation. The current references, i_{d_ref} and i_{q_ref}, are usually generated from the outer power loops, which are not shown in the figure. For analysis simplification, in this paper, i_{d_ref} and i_{q_ref} are considered as adjustable constants needed for output power PQ regulation.

A. Grid-connected System Under Study

The grid-connected system under study is shown in Fig. 2. Here, U_{dc} is the dc-link voltage, L_1 is the converter-side filter inductor, Z_g is the equivalent impedance of the transmission line, i_x with $x = \{a, b, c\}$ is the output current of the GSC, u_c is the converter output voltage, u_{tx} with $x = \{a, b, c\}$ is the voltage at the PCC, e_g is the grid voltage, θ is the PLL output angle, $|u_t|$ is the magnitude of the PCC voltage, K_m, K_f and K_d are modulation, feed-forward and decoupling coefficients, respectively, k_p and k_i are the proportional and integral gain of the current controller respectively, k_{ppll} and k_{ipll} are the

PLL proportional and integral gains. Subscript 'd' denotes for corresponding in d-axis while subscript 'q' denotes for values in q-axis.

B. Impedance Based Analysis of CGI-SSO Mode

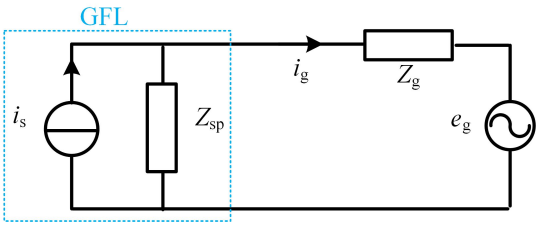

Fig. 3. Impedance model of WT grid-connected system.

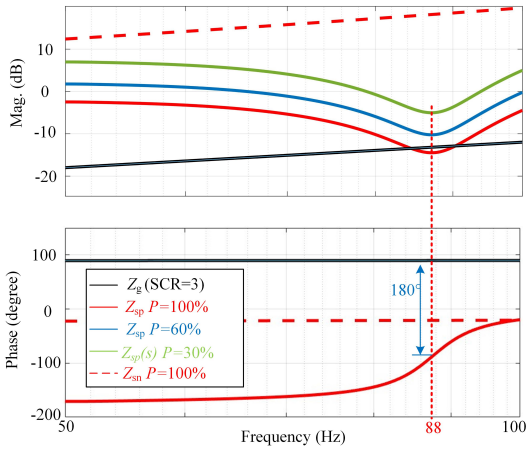

Fig. 4. Frequency characteristic of $Z_{sp}(s)$,$Z_{sn}(s)$ and $Z_g(s)$ under different output power.

Since the principle of GFL converters is to regulate the output current synchronized with the grid voltage, it behaves a current source in parallel with an impedance [6], which is then series connected with the grid voltage through the line impedance $Z_g(s)$. In [19] was proven that the synchronous reference frame-PLL (SRF-PLL) strongly affects the positive-negative sequences output impedance and the stability of grid-tied converters. Research in [12] indicates that the positive-sequence impedance of the WT GSC is enough to judge the stability of the grid-connected system. On these basis, the positive-sequence impedance model of the system is shown in Fig. 3. Here, Z_{sp} and Z_g are the output impedance of WT GSC and the grid impedance, respectively. In Fig. 3, the current injected into the grid can be expressed as:

$$I_g(s) = [I_s(s) - \frac{e_g(s)}{Z_{sp}(s)}]\frac{1}{1 + Z_g(s)/Z_{sp}(s)}. \tag{1}$$

where $Z_{sp}(s)$ is the equivalent positive sequence output impedance of the GFL GSC considering the PLL dynamic, which is expressed as (2), at the bottom of the page.

In (2), $G_i(s)$ and $H_{PLL}(s)$ are the current controller and the PLL control loop gain, respectively expressed as

$$G_i(s) = k_p + \frac{k_i}{s}. \tag{3}$$

$$H_{PLL}(s) = (k_{ppll} + \frac{k_{ipll}}{s})/s. \tag{4}$$

$T_{PLL}(s)$ is the PLL closed loop transfer function and it is expressed as

$$T_{PLL}(s) = V_1 H_{PLL}(s)/[1 + V_1 H_{PLL}(s)]. \tag{5}$$

where V_1 is the magnitude of the PCC voltage. V_{dcref} is the rated dc-side voltage which is equal to the dc-link voltage, f_o is grid fundamental frequency, I_1 and φ_{i1} are the amplitude and phase of the converter output current i, respectively.

$H_i(s)$ and $H_v(s)$ are the sampling and hold model of the voltage and current measurements, respectively. Since this paper mainly focuses on low frequency stability, the digital delay can be neglected to simplify the analysis. More details on the modeling of $Z_{sp}(s)$ can be found in [20].

Assuming that the system can operate stably in stiff-grid condition, then the stability of the grid connected system is determined by the impedance ratio in the right part of (1), expressed as

$$G_r(s) = \frac{Z_g(s)}{Z_{sp}(s)}. \tag{6}$$

With the parameters given in Table I, Fig. 4 shows the frequency response of $Z_g(s)$, $Z_{sp}(s)$ and $Z_{sn}(s)$ under different WT output power. From the figure, $Z_{sp}(s)$ always have a magnitude valley at around 88 Hz. When the WT output power is 30% of the rated power, the valley of $Z_{sp}(s)$ is far away from $Z_g(s)$, indicating good stable margin. When WT output power is increased to 60% of the rated power. In this case, $Z_{sp}(s)$ moves downside and the valley becomes much more closer to the curve of $Z_g(s)$. Since the phase difference between $Z_{sp}(s)$ and Z_g at the magnitude valley of $Z_{sp}(s)$ is around 180°, it implies the risk of a super-synchronous resonance around 88Hz and a sub-synchronous oscillation mode at 12Hz in the abc-frame [21]. Besides, such oscillation modes in the abc-frame will be transformed into a 38Hz sub-synchronous oscillation mode in the dq-frame. With a further increase of the WT output power to 100% of the rated power and the system SCR is calculated around 3, $Z_{sp}(s)$ intersects $Z_g(s)$ at two different frequencies. The left intersection point is at 85Hz with over 180° phase difference. It can be concluded that increasing the WT output power over a certain limit, the converter output impedance is more likely to interact with the grid impedance, leading to worse stability conditions. Therefore, the total output power injected by a

$$Z_{sp}(s) = \frac{K_m V_{dcref}[G_i(s - j2\pi f_0) - jK_d]H_i(s) + sL_1}{1 - K_m K_f V_{dcref} H_v(s) - \{T_1 e^{j\varphi_{T1}} + [G_i(s - j2\pi f_0) - jK_d]I_1 e^{j\varphi_{i1}}\} \times T_{PLL}(s - j2\pi f_0)H_v(s)K_m V_{dcref}/2V_1}. \tag{2}$$

TABLE I
WT GRID-SIDE CONVERTER PARAMETERS

Symbol	Value	Symbol	Value
k_{ppll}	0.11	k_{ipll}	100
k_p	$0.12/(K_m V_{dcref})$	k_i	$2.5/(K_m V_{dcref})$
K_m	0.5	K_d	$0.0314/(K_m V_{dcref})$
K_f	$1/(K_m V_{dcref})$	V_{dcref}	1400 V
L_1	0.1 mH	Z_g	0.4 mH + 0.01Ω
P_N	1.25 MW	V_1	560 V

wind farm into weak-grids might be limited due to SSO issues. Besides, the negative sequence $Z_{sn}(s)$ of GFL converter is also given in Fig. 4. As seen, $Z_{sn}(s)$ is far away from $Z_g(s)$, which means that the negative sequence will not interact with the grid impedance around the frequency region, indicating good stability. Therefore, in the rest part of the paper, only positive sequence is considered for stability analysis.

III. GRID STIFFNESS ENHANCEMENT BY EXTERNAL INTEGRATION OF BESS IN GFM CONTROL MODE

A potential way to damp the SSO is to integrate BESS into the grid-connected system. Generally, there are two methods to integrate BESS into the system: a) external integration of the BESS at the PCC with the combination of a GFM converter; b) integrating BESS inside the WT. In this section, SSO damping contribution from BESS combined with GFM converter (GFM-BESS) is discussed. On the basis, conflicts between SSO damping performance and BESS power rating are discussed, and a coefficient decoupling control method is proposed to realize SSO damping while keeping low BESS power rating.

A. System Impedance Model With Integration of GFM-BESS

The diagram of the WT grid-connected system with integration of external BESS is shown in Fig. 5(a). Basically, a GFM-BESS consists of a battery module, a dc-dc converter and a grid side inverter operating in GFM mode, as shown in Fig. 5(b). To simplify the analysis, the dc-dc converter dynamic is neglected and the dc-link voltage U_{dc} is considered to be constant. Here, L_2 is the inductance of converter side filter, R_s is the equivalent resistance of converter side filter, and it can be also emulated through virtual impedance approach; i_{ex} with $x = \{a, b, c\}$ is the output current of the battery inverter, u_{ec} is the inverter output voltage. According to different control objectives, various kinds of GFM control schemes are available and reviewed in literature [6]. The synchronverter control is selected in this work.

Differently from the output model of the WT converter, the BESS converter behaves equivalently as a voltage source u_s in series with an impedance Z_{vsg} due to the voltage regulation principle, as shown in Fig. 6. Therefore, the integration of GFM-BESS introduces an impedance in parallel with the grid impedance, thus changing the equivalent grid impedance Z_{equ}, expressed as

$$Z_{equ}(s) = Z_{vsg}(s)||Z_g(s) = \frac{Z_{vsg}(s)Z_g(s)}{Z_{vsg}(s) + Z_g(s)}. \quad (7)$$

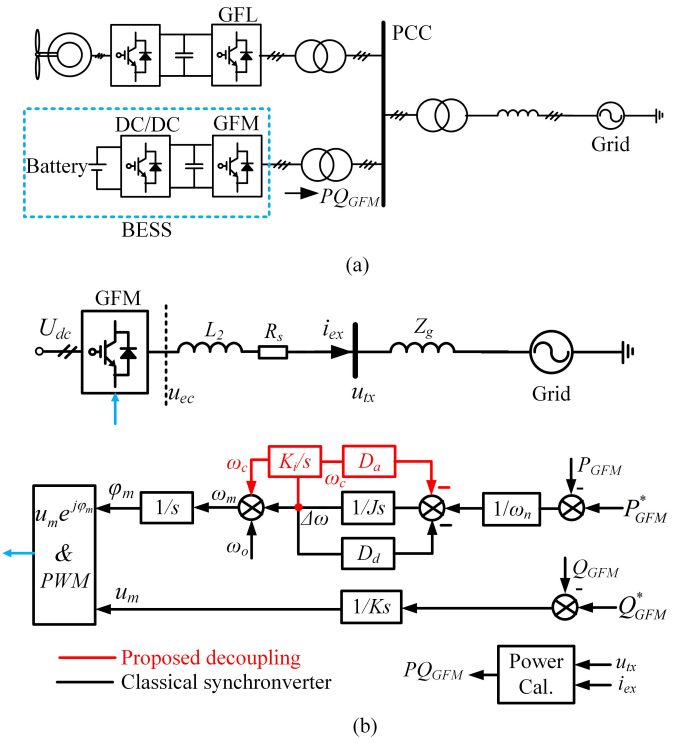

Fig. 5. WT grid-connected system with integration of external GFM-BESS. (a) System diagram. (b) Control diagram of the GFM-BESS.

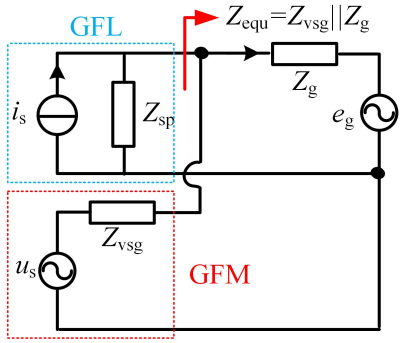

Fig. 6. Impedance model of WT grid-connected system with external BESS.

In (7), $Z_{vsg}(s)$ represents for the equivalent output impedance of the BESS grid-side converter, expressed as

$$Z_{vsg}(s) = \frac{0.75V_1M(s - j\omega_g)K(s)e^{j\varphi_{vir}}/\omega_n + sL_2}{1 + 0.75I_2M(s - j\omega_g)K(s)e^{-j(\varphi_{i,1} - \varphi_{vir})}/\omega_n}, \quad (8)$$

where V_1 is the amplitude of the voltage at the PCC point, I_2 is the amplitude of the GFM output current, while $\varphi_{i,1}$ is the initial phase angle of the current i_e. φ_{vir} is given as

$$\varphi_{vir} = \frac{\pi}{2} + \arcsin(P_{GFM}\omega_n L_2/V_1 E_m), \quad (9)$$

where E_m is the RMS of the virtual-back EMF voltage of GFM-BESS, expressed as E_m=$u_m/\sqrt{2}$. $P_{GFM} \approx P^*_{GFM}$ is the power output of the GFM-BESS under nominal condition, ω_n is the fundamental frequency of PCC voltage u_t. Moreover,

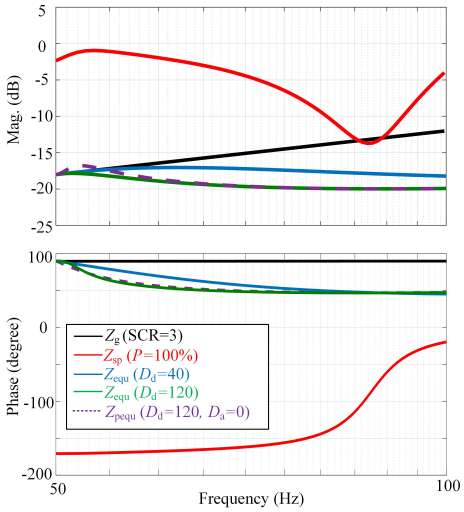

Fig. 7. Frequency characteristic of $Z_{sp}(s)$, $Z_g(s)$ and $Z_{equ}(s)$.

TABLE II
BESS CONVERTER PARAMETERS

Symbol	Value	Symbol	Value
P_{GFM}	0MW	Q_{GFM}	0VAR
K	50	K_i	10
J	0.01	D_d	40 $\sim$ 120
ω_n/ω_o	314	D_a	0
L_2	0.1 mH	R_s	0.1Ω

in (8), $M(s)$ is given as

$$M(s) = \frac{1}{Js^2 + D_d s}, \tag{10}$$

where J is the virtual inertia coefficient and D_d is the damping coefficient. $K(s)$ is given as

$$K(s) = \frac{\sqrt{2}E_m e^{-1.5sT_s}}{(1 + s/\omega_v)(1 + s/\omega_i)}, \tag{11}$$

where ω_v and ω_i are the cutoff angular frequencies of the low-pass filter for the voltage and current measurements respectively, T_s is the switching period. More details on the derivation of $Z_{vsg}(s)$ can be found in [22].

With the parameters given in Table I and Table II, Fig. 7 shows the frequency response of the GFL output impedance Z_{sp}, the grid impedance Z_g, and the equivalent parallel grid impedance Z_{equ} under various damping coefficient D_d values. It can be seen that, if there is no GFM-BESS integrated, an unstable intersection between the Z_g and Z_{sp} appears when the wind power reference P_N is set to 1.25MW (e.g. SCR = 3). The unstable intersection leads to an unstable SSO mode as discussed in Section II-B. With the integration of GFM-BESS at the PCC, the magnitude of the equivalent grid impedance Z_{equ} around the intersection frequency is reduced, indicating a stronger grid from the view of the GFL converter. In this condition, there is no intersection between Z_{equ} and Z_{sp}, which implies an effective SSO damping and stability of the system on one hand. On the other hand, due to a decrease in the magnitude of Z_{equ}, the magnitude of Z_{sp} can be in further decreased before reaching again an unstable intersection with

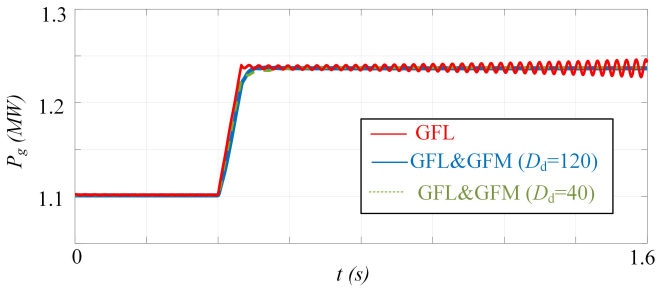

Fig. 8. Simulation results of grid power P_g under different D_d of GFM converter.

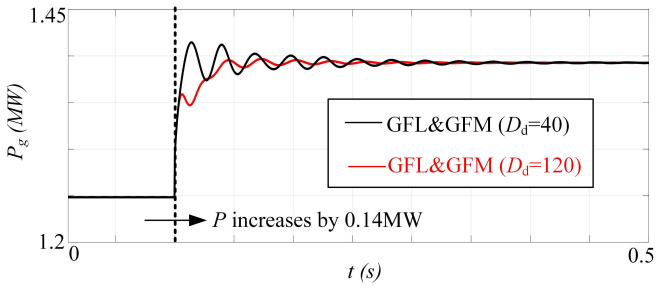

Fig. 9. Dynamic response of grid power P_g under increase of WT power.

Z_{equ}. In other word, more WT power can be transferred stably due to enhanced grid stiffness around the oscillation frequency. It is worth noting that the magnitudes of Z_{equ} and Z_g at 50Hz are almost the same, which means that the transmission capacity is hardly affected whether GFM-BESS is integrated or not. Moreover, when the damping coefficient D_d is increased from 40 to 120, the magnitude of Z_{equ} becomes smaller, providing a better SSO damping and higher WT power inject is enabled.

Fig.8 shows the grid power P_g under different D_d in conventional GFM converter. As seen, when there is not GFM-BESS integrated, the WT reaches the steady-state power P at 1.2MW. When the power reference is set to 1.25MW, the values of P_g starts to oscillate with a frequency around 38Hz and the oscillation tends to diverge, indicating an unstable SSO mode. This SSO mode is essentially originated from the PLL dynamic [2]. With the integration of GFM-BESS, P_g can stably reach 1.25MW, when the damping coefficient D_d of the GFM converter is set in a range between 40 to 120.

Although the integration of GFM-BESS contributes to SSO damping into the system, different damping coefficient contributes to different SSO damping performance. Fig. 9 shows the dynamic response of the grid power P_g under a WT power step. Before $t = 0.1s$, P_g reaches 1.25MW stably with the integration of conventional GFM. At, $t = 0.1s$, the WT power P suddenly increases by 0.14MW, a SSO mode is excited and then damped by the GFM converter. It is found that P_g shows better damped SSO mode when D_d is set to 120. Therefore, by properly increasing the damping coefficient, the SSO mode can be better damped. It is worth noting that the oscillation mode on P_g in this condition shifts to 35Hz as compared to the 38Hz mode shown in Fig. 8, which is due to the change

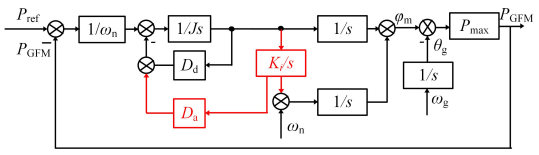

Fig. 10. Active power control diagram of GFM-BESS.

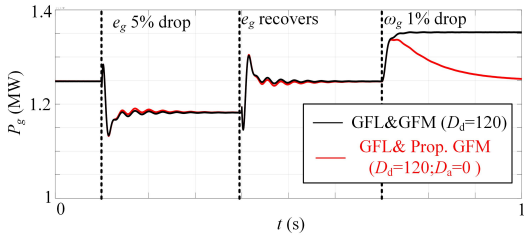

Fig. 11. Dynamic response of grid power P_g under two different GFM control.

of frequency responses of Z_{sp} and Z_{equ} in this case.

B. Coefficient Decoupling Control in Synchronverter GFM

As discussed in the former section, increasing damping coefficient D_d properly helps to provide more SSO damping and more WT output power is enabled in normal operating condition. However, under frequency disturbances, due to the droop meaning of the coefficient D_d, the GFM converter will react to a grid frequency drop by increasing its power output proportionally to the value of D_d, leading to an higher power rating of the BESS, and the realization costs may increases as a consequence. To address this issue, a new control method is proposed in [16] by the authors to decouple the droop and the damping meaning from the coefficient D_d.

The control algorithm can be seen in the red part in Fig. 5(b). The proposed method consists of an additional integrator with gain K_i for the output frequency ω. Basically, ω consists of two components, a dc-component due to the grid frequency deviation from its nominal value (50Hz) and a small-signal disturbance. When the dc-component of ω is not equal to zero, the additional integrator will react and its output ω_c will increase continuously. Since ω_c is also feedforward to the loop for synchronization purpose, its value will not increase infinitely. Under the steady-state, ω_c will be equal to the grid frequency deviation while only disturbance remains in ω. On this basis, Both ω_c and ω can be feedback to the control loop with independent coefficients to modify the converter behaviors. In the manuscript, the droop behaviour of the GFM converter is affected by the droop constant D_a, while the SSO damping is mainly affected by the damping coefficient D_d.

Neglecting the ac voltage magnitude dynamic on the GFM converter model, the control diagram of the proposed method can be simplified as in Fig. 10. Here, ω_g and θ_g are the frequency and angle of the grid voltage, respectively, P_{max} is the power-angle relation between the GFM converter output voltage and the PCC voltage, and it is generally a constant under small-signal conditions. Through the small-signal analysis, the relation between ω_g and P_{GFM} can be expressed as:

$$\frac{\Delta P_{GFM}(s)}{\Delta\omega_g(s)} = \frac{-P_{\max}(Js^2 + D_d s + K_i D_a)}{P_{\max}(s+K_i)/\omega_n + Js^3 + D_d s^2 + K_i D_a s}. \tag{12}$$

According to the final-value theorem applied to (12), the variation of ΔP_{GFM} under grid frequency deviation $\Delta\omega_g$ can be derived as

$$\lim_{t\to\infty}\Delta P(t) = \lim_{s\to 0}\frac{-sP_{\max}(Js^2 + D_d s + K_i D_a)\Delta\omega_g(s)}{P_{\max}(s+K_i)/\omega_n + Js^3 + D_d s^2 + K_i D_a s}, \tag{13}$$

where $\Delta\omega_g(s)$ is expressed as

$$\Delta\omega_g(s) = \frac{\Delta\omega_g}{s}. \tag{14}$$

After few rearrangements, (13) is simplified as

$$\lim_{t\to\infty}\Delta P(t) = -\Delta\omega_g\omega_n D_a. \tag{15}$$

From (15), the droop constant of the proposed method is only determined by the coefficient D_a rather than the damping coefficient D_d, which indicates the decoupling between the damping and the droop coefficients in the GFM control. Since the proposed method is realized by modifying the active power loop on the basis of the conventional synchronverter, it is essentially a GFM control and it can be also modeled as a voltage source behind an output impedance Z_{pvsg} similarly to the impedance model shown in Fig. 5. Therefore, referring to (7)-(11), the equivalent impedance Z_{pvsg} of a GFM-BESS with the proposed decoupling method can be derived as

$$Z_{pvsg}(s) = \frac{0.75V_1 M_p(s-j\omega_g)K(s)e^{j\varphi_{vir}}/\omega_n + sL_2}{1 + 0.75I_2 M_p(s-j\omega_g)K(s)e^{-j(\varphi_{i,1}-\varphi_{vir})}/\omega_n}, \tag{16}$$

where $M_p(s)$ is given as

$$M_p(s) = \frac{s+K_i}{Js^3 + D_d s^2 + K_i D_a s}, \tag{17}$$

as the consequence of the modified active power loop. Substituting Z_{vsg} in (7) with Z_{pvsg} in (16), the expression of the parallel impedance Z_{pequ} can be rewritten as

$$Z_{pequ}(s) = Z_{pvsg}(s)||Z_g(s) = \frac{Z_{pvsg}(s)Z_g(s)}{Z_{pvsg}(s)+Z_g(s)}. \tag{18}$$

On this basis, Fig. 7 in further compares the frequency characteristics of parallel impedance Z_{equ} and Z_{pequ} under different control parameters. In this case, D_a of the proposed method is set to zero while the damping coefficient D_d for both Z_{equ} and Z_{pequ} is set to 120 and the respective SSO damping performance are compared. As seen from the green and purple curves in Fig. 7, the frequency characteristics of Z_{equ} and Z_{pequ} are almost the same in terms of magnitudes and phases within the frequency range between 60Hz-100Hz. This means that the proposed method can realize the same SSO damping behavior as compared to the conventional synchronverter using the same D_d and a small J. It is also valid when the droop coefficient is adjusted to other values. To this extent, Fig. 11 compares the grid power dynamic P_g under two different GFM control methods.

In the figure, sudden changes of the grid voltage and frequency are triggered to test the dynamic of the control system. As shown in Fig. 11, when the damping coefficients in both the methods are set to 120, the transient behaviours of P_g are similar in both the cases, which proves their similar SSO damping contribution. Moreover, the droop coefficient D_a of the proposed method is set to zero. When there is a grid frequency drop (e.g. 1% drop of ω_g), the grid power P_g shows a smaller power peak during the transient while keeping unchanged in the steady-state, under the proposed method. Therefore, the power rating and size of the GFM-BESS can be reduced with the proposed method due to a smaller D_a. Although the proposed method has lower power peak during the transient, the error between the peak value and the steady value of P_g is still high. To address the problem, it is recommended to combine the BESS with super-capacitor to meet the short-term power requirement during the frequency transient [23]. While the BESS is mainly needed for long-term power requirement relevant to D_a.

Besides, the peak of P_g is mainly caused by the inertia synthesis of the proposed control, which will be introduced in the next subsection. Therefore, the proposed GFM control will mainly participate in inertia support. In this condition, the frequency support service provided by the two methods are different while their SSO damping performance are the same.

C. Parameters Design for the Decoupling Control

The last subsection mainly discussed the SSO damping from the GFM converter. However, another important service provided by the GFM converter is the frequency support. Therefore, parameters design of the GFM control are usually aligned with the grid codes, considering both inertia and droop support. In this section, a general parameter design method for droop, inertia and damping of the proposed decoupling control is provided, and the stability and dynamic response of two GFM control methods are compared.

The first step is to design droop coefficient D_a, which refers to

$$D_a = \frac{P_{GN}}{\omega_n^2 K_{df}}, \tag{19}$$

where P_{GN} is the full power of the GFM converter and K_{df} is usually set to 0.03 $\sim$ 0.05 from the grid codes [24], which means that the GFM power should change by P_{GN} when the grid frequency is deviated by 0.03$\sim$ 0.05 of its nominal value. In the manuscript, P_{GN} is designed to be 10% of the GFL nominal power [25] while K_{df} is set to be 0.05, then D_a is designed with 25. Besides, D_a corresponds to D_d of the conventional method.

The second step is to design the inertia. According to [26], synthetic inertia is defined as the controlled contribution of electrical torque from a unit that is proportional to the rate of change of frequency (RoCoF) at the terminals of the unit, which is expressed as

$$\Delta P_e = -J_i \frac{d\Delta\omega}{dt}\omega_n \approx -J_i \omega_{rocof}\omega_n, \tag{20}$$

Where J_i is the inertia and ω_{rocof} is RoCoF. On the basis, the equivalent swing equation of the proposed method is derived as

$$-\frac{d\Delta P_{GFM}}{K_i\omega_n dt} - \frac{\Delta P_{GFM}}{\omega_n} = \frac{Jd^2\Delta\omega_m}{K_i dt^2} + \frac{D_d d\Delta\omega_m}{K_i dt} + D_a\Delta\omega_m. \tag{21}$$

To obtain the inertia, a constant RoCoF is considered at the grid frequency and assuming that the GFM control can track with the frequency deviation well. On the basis, (21) is simplified as:

$$D_a\omega_{rocof} - \frac{K_i\Delta P_{GFM}}{\omega_n} = D_d\omega_{rocof} + K_i D_a\Delta\omega_m. \tag{22}$$

After arrangements, (22) is rewritten as:

$$-\Delta P_{GFM} = (\frac{D_d - D_a}{K_i})\omega_n\omega_{rocof} + D_a\omega_n\Delta\omega_m. \tag{23}$$

From (23), there is an component proportional to the RoCoF. With analogy to (20), the inertia of the proposed method is defined as:

$$J_i = \frac{(D_d - D_a)}{K_i}, \tag{24}$$

where value of J_i refers to the equation

$$J_i = \frac{2HP_{GN}}{\omega_n^2}, \tag{25}$$

where H is inertia constant. when H = 0.4s, J_i is calculated as 1. Besides, J_i corresponds to J of the conventional method.

Furthermore, it can be seen that in the proposed method, the inertia is no longer determined by J but by J_i in (24). To avoid small-signal-stability issues, the value of J can be designed by a small value, e.g., 0.01 in the manuscript.

The next step is to design the damping ratio ξ of the GFM converter. (12) gives the relation between ω_g and P_{GFM}. Through the eigenvalues study, when J is set to a small value, the dominant poles are hardly affected. Therefore, (12) can be simplified as:

$$\frac{\Delta P_{GFM}(s)}{\Delta\omega_g(s)} = \frac{-P_{\max}(D_d s + K_i D_a)}{P_{\max}(s + K_i)/\omega_n + D_d s^2 + K_i D_a s}. \tag{26}$$

By analogy of (26) to a classical second order system, it obtains:

$$\frac{\Delta P_{GFM}(s)}{\Delta\omega_g(s)} = \frac{-P_{\max}(s + K_i D_a/D_d)}{s^2 + 2\xi\omega_a s + {\omega_a}^2}, \tag{27}$$

where ω_a is given by :

$$\omega_a = \sqrt{\frac{P_{\max}K_i}{\omega_n D_d}}. \tag{28}$$

According to (24), inertia J_i is proportional to (D_d-D_a). Therefore, D_d can be designed with a larger value to reduce the weight of D_a on J_i. On the basis, (24) can be approximated as:

$$J_i = \frac{D_d}{K_i} \tag{29}$$

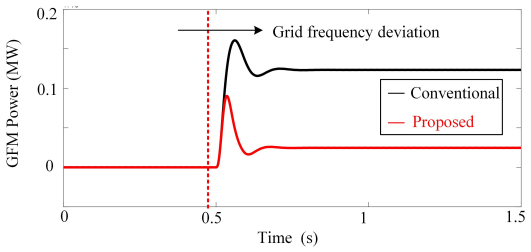

Fig. 12. Power response comparison of two GFM controls to the frequency deviation.

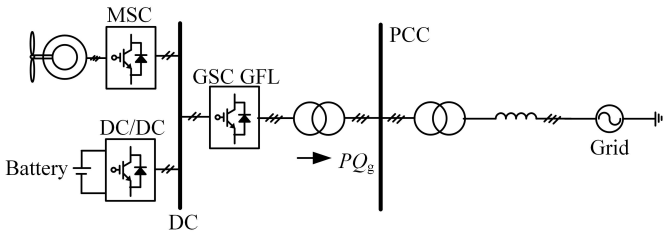

Fig. 13. Structure of D-PMSG based wind turbine grid connected system considering internal BESS.

Substituting (29) to (28), it obtains:

$$\omega_a = \sqrt{\frac{P_{\max}}{\omega_n J_i}}. \tag{30}$$

On the basis, substituting (19) and (30), the damping ratio ξ is given by:

$$\xi = \frac{D_a}{2\omega_a J_i} + \frac{P_{max}}{2\omega_a \omega_n D_d}. \tag{31}$$

As other parameters have already been designed, the damping ratio can be flexible designed by setting different damping coefficient D_d. When ξ is set to 0.6, D_d is calculated as 110.

Since D_d, D_a and J_i have been designed, according to (24), K_i can be calculated as 85.

With the design method, the droop, inertia and damping of the GFM converter can be flexibly tuned. It should be noted that the above analysis assumes that the active power and reactive power of the GFM converter are decoupled. If the power coupling cannot be neglected, the parameter design may not be accurate.

On the basis, power response of two GFM controls to the frequency deviation are compared, as shown in Fig. 12. It's worth noting that for the conventional method, setting J=1 and D_d=25 is not able to keep enough damping for the GFM converter. To solve the problem, damping coefficient D_d is increased to 125 for the same ξ of the proposed method. In Fig. 12(a), a 0.5Hz grid frequency deviation is applied at 0.5s, and two GFM control share the similar power profile during the transient, indicating similar inertia and damping. Under steady state, the proposed method performs far less droop constant, which well aligns with the grid codes.

With the general parameter design method, the proposed method has more flexibility in droop and inertia design for grid codes alignment. While the conventional method has more limitation in droop and inertia design due to the stability problem.

It is worth noted that with the design method, SSO damping of the proposed method will be slightly worse than the conventional method (with higher droop). Because the proposed method has to trade-off between the SSO damping and the grid codes alignment in parameters design. When two methods share the same inertia and the droop constant. SSO damping of the proposed method can be improved by properly increasing J. Although it will reduce the total damping ratio of the GFM converter, the damping can be partly compensated by setting a higher damping ratio reference through the proposed design method and the damping ratio is still better than the conventional method.

IV. Virtual Grid-Forming Control in Wind Turbines with Internal BESS

As discussed in Section III, integrating external GFM-BESS helps to damp the SSO caused by the interaction between WT converters and the grid under weak-grid conditions by changing equivalent grid impedance. Apart from having an external GFM-BESS, [18] discussed the possibility of integrating BESS inside the WT to deal with the intermittent wind energy production and the problem of mismatches between the wind energy generation and the grid demand. The structure of the grid connected system with internal BESS is shown in Fig. 13. Here, the BESS shares the same dc-link with the WT grid-side converter through a dc-dc converter which can be used to either regulate the dc-link voltage or power flow of the WT. Therefore, it is intuitive to use the BESS as a tank to store additional power from the WT generator. As a result, the power transferred into the grid is reduced and unstable SSO might be avoided. An issue of this approach is related to the BESS capacity which is limited and it can not always absorb power from the WT.

As requested by a recent standard of State Grid Corporation of China Enterprise [25], the wind turbine with BESS should provide frequency support to the power system while emulating the inertia and damping of a synchronous machine. However, since the overall power would be processed by the WT converter under GFL control, SSO are expected under weak-grid conditions as already pointed out in Section II. A virtual grid-forming control is proposed and applied to the WT, enabling the WT converter to emulate the output behavior of two parallel converters operating in GFL and GFM modes respectively.

A. Structure of the VGFMC

To let single GFL converter to emulate the dynamic behavior of parallel GFL and GFM converters, without changing the main control structure of the single GFL, one possible way is to add additional current reference for the GFL converter. It is practical since the bandwidth of power synchronization and reactive loop of the GFM converter is smaller than the bandwidth of the GFL converter current control loop.

Therefore, the problem is how to obtain the current reference corresponding to the current output of a real GFM

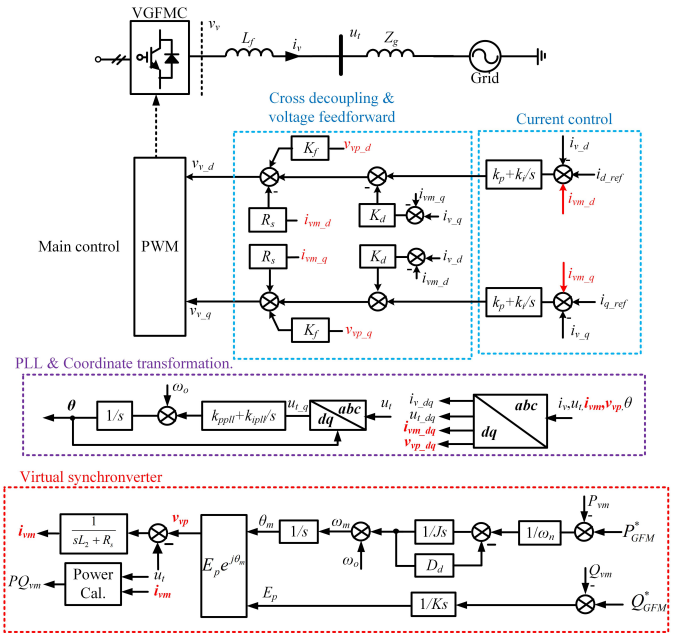

Fig. 14. Control diagram of the VGFMC for the WT converter considering internal BESS.

converter. Because for a single GFL converter, it is impossible to measure the real current of a GFM converter.

To solve this problem, a VGFMC control is proposed in Fig. 14. In the figure, i_v is the converter output current, L_f is the filter inductor and v_v is the converter output voltage. The VGFMC can be divided three blocks:

a) PLL and reference frame transformation: This block uses a PLL to synchronize the converter with the angle and amplitude of the PCC voltage. The output angle θ is then taken as the reference for the abc-dq transformations.

b) Main control: The control is implemented in dq-frame synchronized with the PLL output angle θ. The principle of the block is to regulate the converter output power by controlling the converter output current i_v. The structure of the PLL and the main control block are similar with the classical GFL control shown in Fig. 2.

c) Virtual synchronverter: The structure and parameters of the control block are the same with the synchronverter control given in Fig. 5(b). The differences are that:

1. The error of output voltage of the virtual synchronverter v_{vp} and the PCC voltage u_t passes through a virtual admittance to generate virtual current i_{vm}, expressed as

$$i_{vm\_abc}(s) = [u_{vp\_abc}(s) - u_{t\_abc}(s)]\frac{1}{sL_2 + R_s}; \quad (32)$$

2. The the virtual power PQ_{vm} are calculated through the real PCC voltage u_t and virtual current i_{vm}.

Essentially, the VGFMC is still a kind of GFL control. The differences between the VGFMC and classical GFL are that:

1. i_{vm_dq} from the virtual synchronverter block is taken as additional current reference for the main control block;
2. u_{t_dq} are substituted with v_{vp_dq} from the virtual synchronverter block for voltage feed-forward purpose;

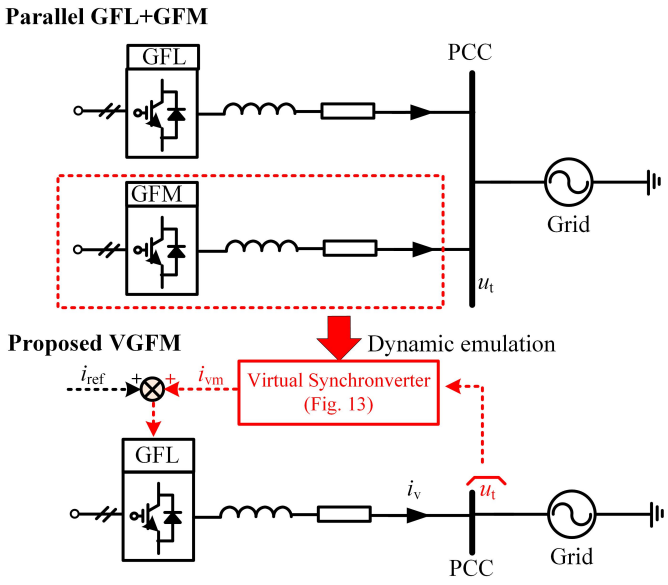

Fig. 15. Illustration of the principle of the virtual synchronverter.

3. Errors between i_{vm_dq} and i_{v_dq} are used for crossing decoupling;
4. i_{vm_dq} are feed-forwarded to the control loops through proportional gain R_s.

It is worth noting that during the transient, the voltage feed-forward and crossing decoupling block can be also flexibly switched to the conventional methods shown in Fig. 2. However, the small-signal stability of the converter would become slightly worse and the reactive power dynamic response to the grid voltage event might be worse.

From (32), it can be concluded that with a virtual synchronverter it is not necessary to have a real GFM converter to interact with the PCC voltage and provide SSO damping. Instead, a real GFM converter output current dynamic can be emulated inside the digital controller with a virtual synchronverter block, as shown in Fig. 15. Then, a virtual current i_{vm} is generated and taken as additional reference for the current loop. This raises the question of how accurate the (32) is at emulating the current dynamics of a real GFM converter. Therefore, in [27], the authors studied the dynamics of GFM converters whose power is calculated by the real current and the virtual current. The results showed that the dynamics of the two methods are similar, especially under weak grid conditions. Therefore, it is reasonable to assume that the GFL current loop can always track the reference GFM current with fast dynamics and high accuracy.

As the consequence, the real output current i_v will consist of two components:

1. i_{ref}, originated from the outer loop of the conventional GFL control such as dc-link voltage controller;
2. i_{vm}, originated from the virtual synchronverter loop, which is similar to the output current of a real GFM converter using the same control parameters.

Consequently, from the view of the grid, the current injected into the grid is likely to come from two parallel converters

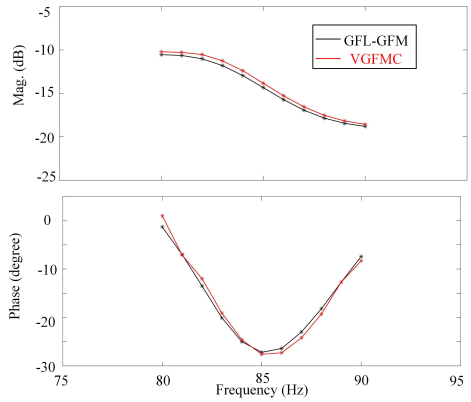

Fig. 16. Measured impedance of GFL-GFM and VGFM.

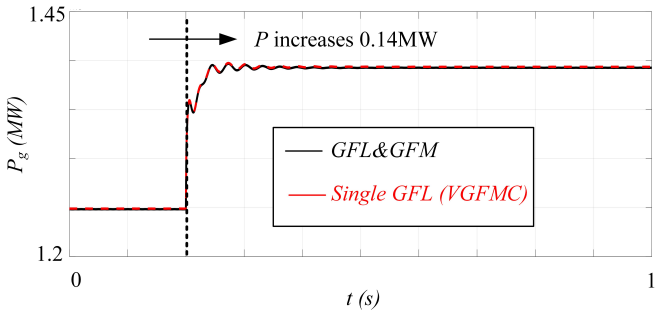

Fig. 17. Comparison of active power P_g injected into grid under two different BESS integration approaches.

which operate in GFL and GFM control respectively. However, there is only one converter implemented with the VGFMC. That is the reason why the method is called VGFMC because there is not a real GFM converter connected at PCC but its output behavior is emulated through control approach. Since the VGFMC emulates the output behavior of a real GFM converter, SSO damping performance similar to the one obtained with an external GFM converter could be realized.

B. SSO Damping Comparison with Conventional Parallel Converters

The measured impedance plot of parallel GFL-GFM converters and VGFM converter around the focused frequency are shown in Fig 16. It can be found that the VGFM and GFL-GFM share the similar impedance plot, which means that the VGFM can emulate similar output behavior of parallel GFL-GFM converters. Therefore, the SSO damping of the system should be also the same.

The SSO damping contribution of the VGFMC is validated and compared to the external GFM converter case in this section. For the external BESS-GFM converter condition, the system consists of a WT in GFL mode and an external BESS in GFM mode, and the overall diagram is shown in Fig. 5. For the VGFMC converter, the BESS is integrated inside the WT, as shown in Fig. 14. Besides, these two approaches share the same control and system parameters given in Table I and Table II.

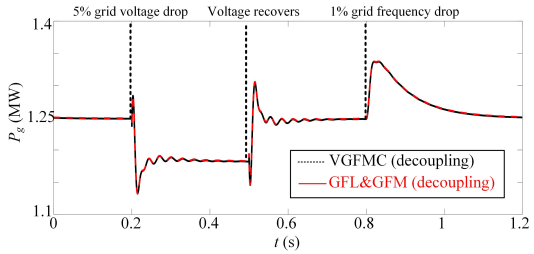

Fig. 18. Dynamics of grid active power P_g under grid events when coefficient decoupling control is applied.

On this basis, Fig. 17 shows the simulation results under two different BESS integration approaches when active power P_g is injected into grid with a step function. Before $t = 0.2s$, both the approaches can realize stable operation with a power injection of $P = 1.25$MW. When a $t = 0.2s$ the injected power P is increased by 0.14MW, it can be seen that both the approaches have similar grid power profiles P_g, indicating that the proposed VGFMC can emulate the output behaviors of parallel GFL and GFM converters.

Moreover, a SSO mode is excited and damped under both the approaches, proving that the proposed VGFMC can also emulate the SSO damping contribution of a real GFM converter.

C. Dynamic Comparison Between VGFMC and Conventional Parallel Converters

To further validate the effectiveness and the accuracy of the proposed VGFMC, the grid active power behaviours P_g under two BESS integration approaches are compared in simulation. The system parameters are given in Table I and Table II.

The proposed coefficient decoupling control is applied to the external GFM converter and to the VGFMC converter for transients comparison. In this condition, the damping coefficient D_d is set to 120 to realize good SSO damping performance, while the droop coefficient D_a is set to zero. Fig. 18 shows the grid active power P_g behaviour under several grid events (e.g. 5% grid voltage drop, voltage recovery, 1% grid frequency drop) when the coefficient decoupling control is applied. It is found that both the approaches have similar dynamics on P_g during the transients. Especially, P_g keeps its values unchanged under the grid frequency drop event, which proves that the VGFMC can also emulate the behavior of the proposed coefficient decoupling control.

V. Experimental Results

In this section, the SSO damping capability, droop performances of the proposed decoupling control and VGFMC dynamic are experimentally validated in a small-scale setup. The experimental setup consists of a power amplifier and a Real-Time Digital Simulator (RTDS) to emulate the power grid, a dSPACE MicroLabBox control platform for control implementation, two parallel converters, and a series of inductors to emulate weak-grid, as shown in Fig. 19. The two converters are separately supplied by independent dc-sources, and implemented with conventional GFL and GFM

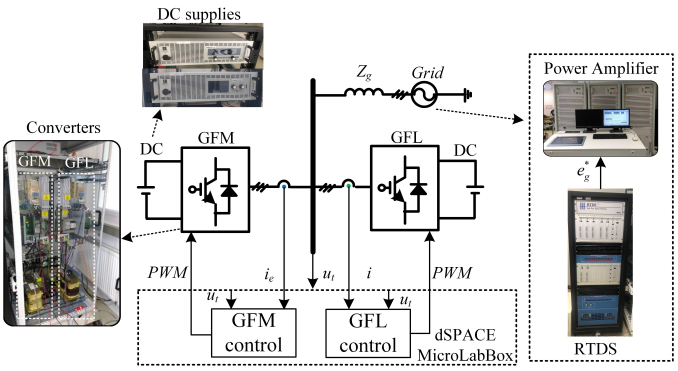

Fig. 19. Photograph and system structure of the setup.

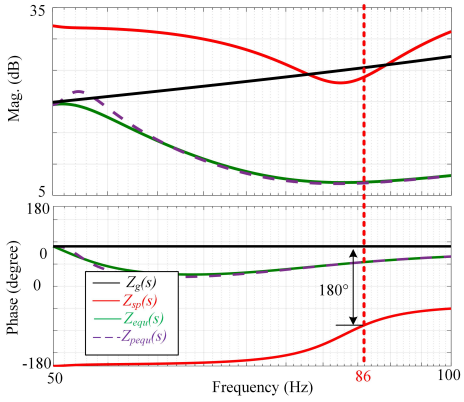

Fig. 20. Frequency characteristic of $Z_{sp}(s)$, $Z_g(s)$, $Z_{equ}(s)$ and $Z_{pequ}(s)$.

respectively. Besides, the system and the controller parameters are scaled down and shown in Table III.

With the parameters given in Table III, Fig. 20 shows the frequency characteristic of $Z_{sp}(s)$, $Z_g(s)$, $Z_{equ}(s)$ and $Z_{pequ}(s)$. It can be seen that the 180° phase difference between $Z_{sp}(s)$ and $Z_g(s)$ is around 86Hz, indicating sub-synchronous oscillation around this frequency region. Considering the integration of the external GFM-BESS without or with the decoupling control, the equivalent grid impedance $Z_{equ}(s)$ and $Z_{pequ}(s)$ moves far away from $Z_{sp}(s)$ at is this frequency region, contributing to SSO damping.

A. *Verification of the SSO Damping with External GFM-BESS*

Fig. 21 shows the output power P and the PLL frequency in the GFL converter when any GFM-BESS is integrated into the system. Before $t = 1.8s$, the GFL converter operates stably with an output power $P = 1.54$kW, while the SCR is calculated around 2 indicating a weak-grid condition. Then the output power is slightly increased from $P = 1.54$kW to $P = 1.61$kW. In this condition, the output power P and the PLL frequency start to oscillate with a 35Hz unstable oscillation mode, until the hardware protections are triggered and the converter is blocked. The oscillating phenomenon basically matches with the impedance analysis shown in Fig. 20, proving the correctness of the impedance model for SSO analysis. The slight difference of oscillation frequency may be due to the resistive components in the system such as grid inductor resistance, which is neglected in the study and will shift the frequency at 180° phase difference.

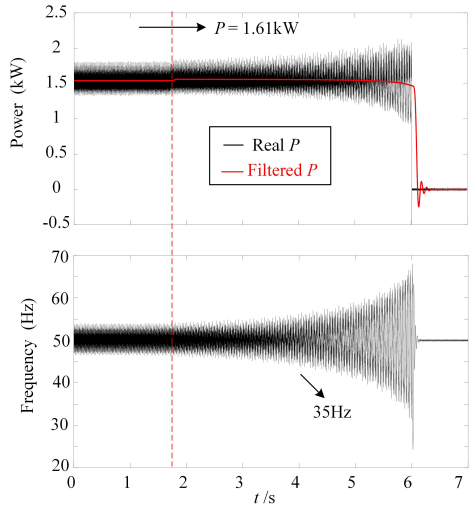

Fig. 21. Output frequency of PLL and power output of the GFL converter without external GFM-BESS converter.

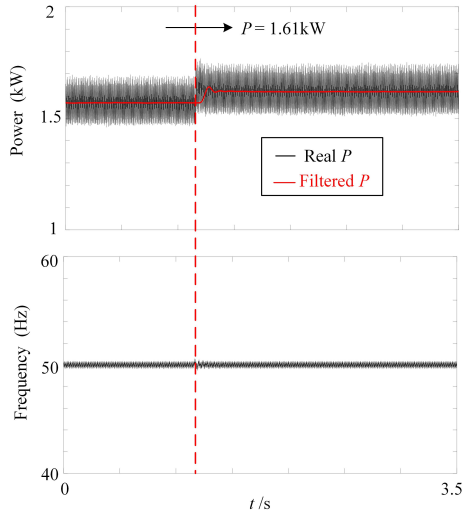

Fig. 22. Output frequency of PLL and power output of the GFL converter with external GFM-BESS converter.

To damp the oscillation and enable the system for higher output power, an external GFM-BESS is integrated at the PCC. Fig. 22 shows the output power and output frequency of PLL of the GFL converter in this condition. Similarly, at $t = 1.8s$, the GFL converter output power increases from $P = 1.54$kW to $P = 1.61$kW. In this case, the new power reference is correctly tracked in a stable operation, and the PLL frequency recovers to the steady-state condition after a short transient. Those results validate that with the integration of GFM-BESS, the SSO oscillation due to the interaction between GFL converter and grid impedance can be well damped and higher output power is enabled.

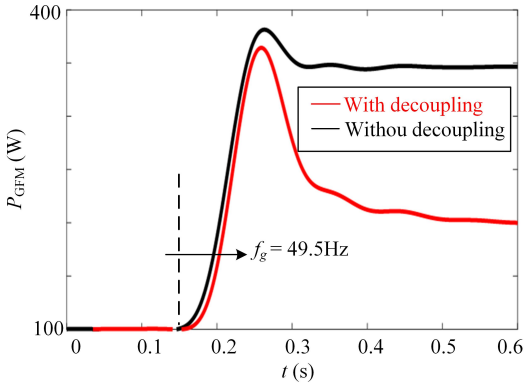

Fig. 23. Power response of the synchronverter with or without decoupling.

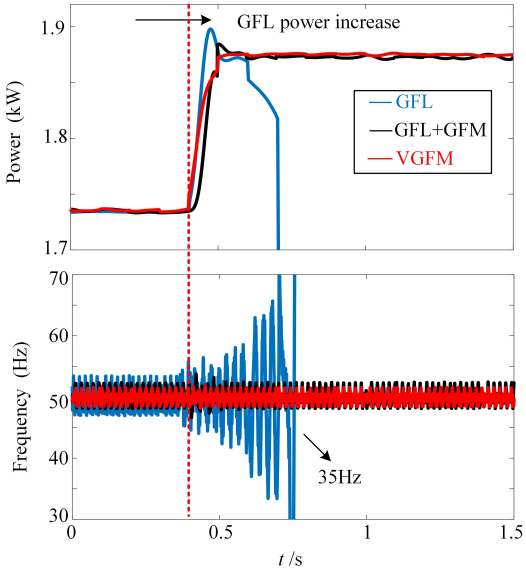

Fig. 24. Experiment results under three cases. (a) Power injected into the grid. (b) PLL frequency.

B. Power Response Under Frequency Deviation

In this section, the power responses of the GFM-BESS converter to a grid frequency deviation under two GFM control strategies (without and with decoupling control) are experimentally obtained and compared, as shown in Fig. 23. At $t = 0.15$s, the grid frequency drops from $f_g = 50$Hz to $f_g = 49.5$Hz. It can be found that the proposed droop-damping decoupling method realizes a lower transient power-peak during and a lower output power in steady-state due to lower adopted droop coefficient D_a, validating the analytical findings in the above sections.

C. Stability comparison between GFL-GFM and VGFM

The experiment result comparison between parallel converters and the proposed VGFM converter are given. The power injected into the grid and the PLL frequency are tested and compared under three different cases,i.e., single GFL converter, parallel GFL and GFM converters and single converter with VGFMC. For each case, the GFL converter is operating close to the critical point and will be turned to instability by a step increase of its output power. The power output of GFM converter is set to be 100W to avoid potential back power flow.

TABLE III
SMALL-SCALE SETUP PARAMETERS

Symbol	Value	Symbol	Value
P_{GFM}	100W	Q_{GFM}	0Var
K	50	K_i	10
J	0.001	D_d	0.25
f_o	50Hz	D_a	0.1
L_2	5 mH	C_f	2.2 μF
k_{ppll}	0.6	k_{ipll}	300
k_p	$18/K_mV_{dcref}$	k_i	$180/K_mV_{dcref}$
K_f	$1/K_mV_{dcref}$	K_d	$1.57/K_mV_{dcref}$
f_s	10kHz	V_{dcref}	700 V
L_1	5 mH	Z_g	30 mH
P	1.62 kW	V_1	150 V

On the basis, experiment results of grid power and the GFL converter PLL frequency under three cases are given in Fig.24. It can be seen that before step change of GFL power, system can operate stably under three cases . It's worth noting that the power plot of single GFL converter case is shifted by 100W to align with the power output of other two cases which have additional power from the GFM converter or VGFM.

A step power increase is applied, and the system becomes unstable when only single GFL converter is connected to the grid, and the oscillation can be observed in the PLL output frequency (active power is filtered by the digital filter). For the cases of parallel converters or single converter case with VGFM control, it can be seen that the grid power can stably reach to the new operating point and the PLL frequency recovers to steady state after a short transient, which indicate improved stability compared to the single GFL case. Moreover, it can be also found that the output power of parallel converters case and the VGFM converter case have similar dynamic during the transient, which prove that the proposed method can emulate the dynamic behavior of parallel converters which operate in GFL mode and GFM mode respectively.

VI. CONCLUSIONS

In this paper, control-based improvements for WF SSO damping with integration of BESS are proposed, considering both external integration case and internal integration case. For the external case, it is revealed that SSO damping can be realized by changing the equivalent grid impedance with the integration of an external GFM-BESS at the PCC of the WT. The SSO damping improvement from a proper increase of the damping coefficient in a synchronverter based GFM control is then proved, though leading to higher power rating requirement for the BESS. A coefficient decoupling control is proposed to decouple the damping and the droop coefficient in a synchronverter based GFM control, leading to lower BESS power rating requirements and similar SSO damping performances. For the approach that integrates GFM-BESS inside the WT, a virtual GFM control for the WT converter is proposed to emulate similar output behaviour of two parallel converters controlled in GFL and GFM modes respectively.

As a result, similar SSO damping contribution and frequency response of an external GFM-BESS can be emulated by wind turbine with the virtual GFM control, without requiring external converters for the BESS. Simulation and experimental results validated that the integration of external GFM-BESS helps to damp the SSO, which can be further emulated through the virtual GFM control for the internal integration case.

ACKNOWLEDGMENT

This work was supported by the European Union's Horizon 2020 Research and Innovation Programme under the Marie Sklodowska-Curie under Grant 861398.

REFERENCES

[1] V. Sewdien, X. Wang, J. Rueda Torres, and M. van der Meijden, "Critical review of mitigation solutions for sso in modern transmission grids," *Energies*, vol. 13, no. 13, p. 3449, 2020.

[2] L. Fan, Z. Miao, S. Shah, Y. Cheng, J. Rose, S.-H. Huang, B. Pal, X. Xie, N. Modi, S. Wang, and S. Zhu, "Real-world 20-hz ibr subsynchronous oscillations: Signatures and mechanism analysis," *IEEE Transactions on Energy Conversion*, pp. 1–11, 2022.

[3] Y. Huang, X. Yuan, J. Hu, and P. Zhou, "Modeling of vsc connected to weak grid for stability analysis of dc-link voltage control," *IEEE Journal of Emerging and Selected Topics in Power Electronics*, vol. 3, no. 4, pp. 1193–1204, 2015.

[4] H. Liu, X. Xie, J. He, T. Xu, Z. Yu, C. Wang, and C. Zhang, "Subsynchronous interaction between direct-drive pmsg based wind farms and weak ac networks," *IEEE Transactions on Power Systems*, vol. 32, no. 6, pp. 4708–4720, 2017.

[5] J. Z. Zhou, H. Ding, S. Fan, Y. Zhang, and A. M. Gole, "Impact of short-circuit ratio and phase-locked-loop parameters on the small-signal behavior of a vsc-hvdc converter," *IEEE Transactions on Power Delivery*, vol. 29, no. 5, pp. 2287–2296, 2014.

[6] R. Rosso, X. Wang, M. Liserre, X. Lu, and S. Engelken, "Grid-forming converters: Control approaches, grid-synchronization, and future trends—a review," *IEEE Open Journal of Industry Applications*, vol. 2, pp. 93–109, 2021.

[7] Z. Kustanovich, S. Shivratri, H. Yin, F. Reissner, and G. Weiss, "Synchronverters with fast current loops," *IEEE Transactions on Industrial Electronics*, pp. 1–10, 2022.

[8] J. Rocabert, A. Luna, F. Blaabjerg, and P. Rodríguez, "Control of power converters in ac microgrids," *IEEE Transactions on Power Electronics*, vol. 27, no. 11, pp. 4734–4749, 2012.

[9] M. Liserre, M. A. Perez, M. Langwasser, C. A. Rojas, and Z. Zhou, "Unlocking the hidden capacity of the electrical grid through smart transformer and smart transmission," *Proceedings of the IEEE*, pp. 1–17, 2022.

[10] X. Xie, H. Liu, J. He, C. Zhang, and Y. Qiao, "Mechanism and characteristics of subsynchronous oscillation caused by the interaction between full-converter wind turbines and ac systems," *Proc. CSEE*, vol. 36, no. 9, pp. 2366–2372, 2016.

[11] Y. Xu, S. Zhao, Y. Cao, and K. Sun, "Understanding subsynchronous oscillations in dfig-based wind farms without series compensation," *IEEE Access*, vol. 7, pp. 107 201–107 210, 2019.

[12] G. Li, Y. Chen, A. Luo, and H. Wang, "An enhancing grid stiffness control strategy of statcom/bess for damping sub-synchronous resonance in wind farm connected to weak grid," *IEEE Transactions on Industrial informatics*, vol. 16, no. 9, pp. 5835–5845, 2019.

[13] S. K. Chaudhary, R. Teodorescu, J. R. Svensson, Ł. H. Kocewiak, P. Johnson, and B. Berggren, "Black start service from offshore wind power plant using ibess," in *2021 IEEE Madrid PowerTech*. IEEE, 2021, pp. 1–6.

[14] S. Cherevatskiy, S. Sproul, S. Zabihi, R. Korte, H. Klingenberg, B. Buchholz, and A. Oudalov, "Grid forming energy storage system addresses challenges of grids with high penetration of renewables (a case study)," in *Proc. CIGRÉ Session*, vol. 2, 2020, p. 322.

[15] V. Mallemaci, F. Mandrile, S. Rubino, A. Mazza, E. Carpaneto, and R. Bojoi, "A comprehensive comparison of Virtual Synchronous Generators with focus on virtual inertia and frequency regulation," *Electric Power Systems Research*, vol. 201, p. 107516, Dec. 2021.

[16] Z. Zhou, S. Pugliese, M. Langwasser, and M. Liserre, "Sub-synchronous damping by battery storage system in grid forming control mode," in *2022 IEEE Energy Conversion Congress and Exposition (ECCE)*, 2022, pp. 1–8.

[17] H. Wu, X. Ruan, D. Yang, X. Chen, W. Zhao, Z. Lv, and Q.-C. Zhong, "Small-signal modeling and parameters design for virtual synchronous generators," *IEEE Transactions on Industrial Electronics*, vol. 63, no. 7, pp. 4292–4303, 2016.

[18] J. Simpson, G. Hanrahan, E. Loth, G. Koenig, and D. Sadoway, "Liquid metal battery storage in an offshore wind turbine: Concept and economic analysis," *Renewable and Sustainable Energy Reviews*, vol. 149, p. 111387, oct 2021.

[19] S. Pugliese, Y. Kwon, and M. Liserre, "Positive-negative sequence srf-pll model for accurate stability analysis in grid-tied converters," in *2020 IEEE Energy Conversion Congress and Exposition (ECCE)*, 2020, pp. 3593–3600.

[20] M. Cespedes and J. Sun, "Impedance modeling and analysis of grid-connected voltage-source converters," *IEEE Transactions on Power Electronics*, vol. 29, no. 3, pp. 1254–1261, 2014.

[21] T. Bi, J. Li, P. Zhang, E. Mitchell-Colgan, and S. Xiao, "Study on response characteristics of grid-side converter controller of pmsg to sub-synchronous frequency component," *IET renewable power generation*, vol. 11, no. 7, pp. 966–972, 2017.

[22] W. Wu, L. Zhou, Y. Chen, A. Luo, Y. Dong, X. Zhou, Q. Xu, L. Yang, and J. M. Guerrero, "Sequence-impedance-based stability comparison between vsgs and traditional grid-connected inverters," *IEEE Transactions on Power Electronics*, vol. 34, no. 1, pp. 46–52, 2019.

[23] D. Lemian and F. Bode, "Battery-supercapacitor energy storage systems for electrical vehicles: A review," *Energies*, vol. 15, no. 15, p. 5683, 2022.

[24] "Ieee standard for interconnection and interoperability of distributed energy resources with associated electric power systems interfaces," *IEEE Std 1547-2018 (Revision of IEEE Std 1547-2003)*, pp. 1–138, 2018.

[25] Q/GDW 11826-2018, "Technical requirement and test methods for wind turbine virtual synchronous generator," State Grid Corporation of China Enterprise Standard, 2018.

[26] R. Eriksson, N. Modig, and K. Elkington, "Synthetic inertia versus fast frequency response: a definition," *IET renewable power generation*, vol. 12, no. 5, pp. 507–514, 2018.

[27] Z. Zhou, S. Pugliese, and M. Liserre, "Stability comparison of grid-forming converters with different power calculation strategies," in *2023 IEEE 14th International Symposium on Power Electronics for Distributed Generation Systems (PEDG)*, 2023, pp. 800–805.